Novel self-similar re-entrant auxetic metamaterials (SREAM): Design, mechanical property, and geometric optimization

Peng Dong [a], Runsheng Hou [a], Jiayi Hu [a], Chen Lin [b], Yuqing Liu [c,*], Lei Qin [d,**]

[a] *Shenzhen Key Laboratory of Soft Mechanics & Smart Manufacturing, Department of Mechanics and Aerospace Engineering, Southern University of Science and Technology, Shenzhen, 518055, China*
[b] *Department of Manufacturing and Civil Engineering, Norwegian University of Science and Technology (NTNU), Teknologiveien 22, 2815, Gjøvik, Norway*
[c] *School of Transportation, Civil Engineering & Architecture, Foshan University, Foshan, 528225, China*
[d] *School of Civil Engineering and Architecture, University of Jinan, Jinan, 250022, China*

A B S T R A C T

In this study, a novel self-similar re-entrant auxetic metamaterial (SREAM) was designed to improve its mechanical performance compared with the conventional re-entrant structure (CRS). Experimental and numerical analyses were carried out to investigate their mechanical performance under quasi-static compression. The mechanical effects of key geometric parameters of inner re-entrants have also been symmetrically investigated to provide the modeling basis for SREAMs' geometric optimization. It was found that SREAM do well in both stiffness and auxeticity simultaneously. The mechanical performance of SREAMs is highly adjustable via proper configuration on geometric parameters. The proposed SREAM possibly provides superior auxeticity and high stiffness, with adjustable performance.

1. Introduction

Auxetic mechanical metamaterials (AAMs) exhibit extraordinary negative Poisson's ratio (NPR) properties because of their unique cellular auxetic geometric configurations. According to their geometric designs, typical AAMs can be divided into several types, such as re-entrants [1], honeycomb [2–4], chiral [5,6], lozenge, and origami [7, 8]. These auxetics show a significant lateral contraction under vertical compression, whereas they present a transverse shrinkage during tension. Such unusual deformation helps achieve the superior mechanical performance of AAMs in terms of energy absorption [9–11], shear resistance [12], negative stiffness [13,14], and fracture resistance [15], thereby gaining potential applications in smart materials, dowels [16], medical implants [17], fasteners, and automotive engineering [18].

As a branch of auxetic metamaterials, conventional re-entrant structure (CRS) has gained more attention due to its superior auxeticity, mechanical performance [19], and flexible geometrical schematics. According to Liu et al. [20], the typical CRS may show a higher energy dissipation property under the dynamic crushing tests than a hexagonal topology. Qi et al. [21] designed a novel 3D re-entrant honeycomb with superior crushing performance under low- and high-speed crushing tests. Zhang et al. [22] proposed another derivative re-entrant honeycomb as cylindrical meta-structure tubes. Such new asymmetrical re-entrant metamaterials show promising auxeticity under quasi-static compression. Other studies may also focus on the mechanical behavior of re-entrants in multiple boundary conditions and loading modes, such as incline loading [23], quasi-static crushing [24], and in-plane impact [25]. Prosperity can be seen in terms of the practical applications of CRS, such as the anti-collision fence, dowel, bumper, and even smart wearable devices, considering the aforementioned superior properties.

Although CRS presents good potential in both properties and applications, there are instinctive defects hindering its development. Being a typical cellular structure, excessive porosity may diminish the overall stiffness of CRS [26], hence limiting its applicability in structural, mechanical, and other domains where stiffness is of paramount importance. Firstly, a possible consequence of the diminished stiffness is that CRS may exhibit a lower level of strength, which could affect its bearing capacity as a structural component. For instance, Cheng et al. [27] presented the typical collapse of steel-made CRS due to low structural stiffness, along with limited compression strength and restricted energy absorption performance. Another issue is that CRS manufactured from flexible materials with viscoelasticity or hyper-elastic properties are

---

prone to exhibit structural instability due to their diminished stiffness. It may further cause undesired mechanical responses, namely, buckling, collapse, and stress concentration. For example, Zhang et al. [28] revealed the typical buckling behavior of CRS under quasi-static compression, where the high cellular CRS topology obviously weakened the stiffness and caused unstable deformation modes. The aforementioned disadvantages of CRS inevitably make its popularization and deployment challenging, particularly for specific application scenarios with unique requirements, such as ultrasensitive intelligent sensing equipment, high security required civil constructions, etc.

As a result, considerable studies concentrated on ways to enhance the stiffness, i.e., the effective Young's modulus. Ruan et al. [29] proposed an innovative antichiral-reentrant hybrid intravascular stent combining the synergistic mechanical benefits of chiral and reentrant structures. Lu et al. [30] proposed a modified re-entrant structure with each unit cell topology adding a narrow rib in the well-known re-entrant cellular structure. The analytical and numerical study showed a consistently enhanced strength and Young's modulus. By changing the basic CRS configurations, specifically adding the extra parts or replacing partial components, geometric modifications such as hybrid [31–33], ribbing [34,35], sandwich [36,37], and optimization [38–40] may produce more innovative structures with high stiffness. Finally, the prosperity of new CRS structures has promoted their applications in various fields [41–44].

However, there are still two main problems when enhancing the stiffness via the aforesaid geometric rebuilding and modifications. First, it should be emphasized that the stiffness and auxeticity of CRS may often conflict with each other. Although excessively materializing the empty regions of CRS shall produce composites with enhanced stiffness, it may result in a distinct decline in auxeticity. Furthermore, it may hinder the application of CRS where the negative poison's ratio property is of equal significance to the specific strength in the large deformation process. It is indeed necessary to make an appropriate compromise between the stiffness and NPR. Apart from making such balance, it is also expected to achieve a high degree of tunable stiffness for the newly produced structure used in various conditions. The structure with tunable stiffness may have better adaptability due to its more flexible mechanical responses, especially in conditions where safety and sensitivity are highly concerned. For instance, soft robotics with adjustable stiffness may achieve a good human-machine interaction performance due to its better safety than rigid robotic arms. To solve the above problems, previous research [45] has paid more attention to achieving a tunable enhanced stiffness by optimizing geometric designs or materials [46]. By employing 4D printing technology, H. Yousuf et al. [47] enable the CRS to obtain a wide-range stiffness ranging from 0.179 to 0.242 kN/mm while collecting the in-plane Poisson's ratio from −0.33 to +0.69. Cheng et al. designed a novel CRS with tunable stiffness following a variable stiffness factor (VSF) method, and the results presented its both consistent auxetic properties and self-adjusting stiffness.

Although many efforts [42,48–51] have been paid to solve the aforesaid problems, the geometric concept of self-similarity is now gaining special attention. In the first place, it has already been proven to achieve high efficiency in stiffness enhancement while keeping superior auxeticity simultaneously. For instance, Lin et al. [52] conducted numerical studies on a self-similar auxetic star honeycomb structure, and the result reveals it obtains an improved energy absorption performance while maintaining superior negative Poisson's ratio property under impact. Another issue is that the self-similar structure could present a highly adjustable stiffness. One typical example concerns the natural self-similar structures that may perform well in resisting various natural enemies and environments. Inspired by coconut palm, for example, Jiang et al. [53] proposed a self-similar concentric auxetic re-entrant honeycomb (CARH) whose geometry consists of two concentric re-entrants. And such bio-inspired design has helped CARH gain a relatively superior crashworthiness at around 258.9% higher mean crushing stress than CRS. Apart from the enhancement effect, it may

offer a more universal geometric design strategy rather than being constrained by a certain initial geometry. In other words, the self-similar geometries may be more compatible with each other and rarely limited to one certain topology. Contrarily, it may be challenging only by introducing or replacing simple components [54] in other geometries like chiral outer, although it did a superior job of the expected tunable stiffness in CRS.

Inspired by the concept of self-similarity, this study introduces a type of novel self-similar re-entrant auxetic metamaterial (SREAM) to achieve a good balance between tunable enhanced stiffness and auxeticity. To compare the mechanical behavior of SREAM and the CRS, a quasi-static compression test was conducted. Herein, the deformation and strain distribution, and the equivalent Young's modulus of the above structures were tracked and computed via a digital image correlation (DIC) technique and FEM methods. Subsequently, the experimental results were verified by a numerical simulation using the commercial numerical software Abaqus. The mechanical effects of vital geometric parameters, namely the thickness, lateral pitch, height, and connection of inner re-entrants for corresponding SREAMs, were discussed to provide possible geometric optimization solutions.

2. Methods

2.1. Geometric design

Fig. 1 presents the geometric schematics of the proposed SREAM-# and the CRS. As shown in Fig. 1(a), each CRS unit can be completely defined by the following parameters: the unit's horizontal side $w = 36$ mm, the unit's height $h = 24$ mm, the thickness of the inclined strut $t = 2.29$ mm, and the included angle $\alpha = 45°$. Based on the concept of self-similarity, the geometry of the proposed SREAM-# (Fig. 1(b)) may consist of two similar parts: the outer re-entrant structure and the nested re-entrant structure. The shape of outer re-entrants is totally the same as CRS in Fig. 1(a), with the same thickness ($t = 2.29$ mm) for all sides or corners. For the nested part in Fig. 1(b), it is composed of two fan blades separated from each other, showing a trend of mutual clasp in the horizontal direction. Compared with two trusses directly opposite each other, hinges may help the two parts transversely contract tightly because of the larger surface area. Such an enlarged surface may offer better geometric tolerance while rarely boosting rotations of the two sides around the hinge center. This is due to the fact that the vertical trusses of the nested re-entrant shall be compacted immediately after the closure, severely limiting the possible rotations, as illustrated in Fig. 4. The specific geometric parameters of this part are defined as follows: the diameter of the hinge $d = 3$ mm, the vertical distance between the two hinges $g = 0.86$ mm, the height of each nested unit $= 14.49$ mm, and the width of each unit $= 19.07$ mm. Besides, to keep shape similarity, the included angle β between sides h and w keep constant at 45°. According to Fig. 1 (a) and (c–e), the size of each unit cell of both SREAM-# and CRS is set constant as $w \times h = 36 \times 24$ mm, and their total dimension is kept as $W \times H = 180 \times 120$ mm.

2.2. Materials and manufacturing

The above specimens in Fig. 1 were fabricated by the Fused Deposition Modeling (FDM) method using a 3D printer (Ender-5, Creality). A type of commercial TPU (Thermoplastic Polyurethane) was used with a filament size of 1.75 mm. To investigate its mechanical property, the dumbbell-shaped TPU samples were also prepared in the specific dimensions (Fig. 2(a)) and tested via a tension test (Fig. 2(b)) according to ASTM D412-16. The hyperelastic properties of the proposed TPU were thus presented in Fig. 2(c). During the printing process, the raw filaments were squeezed through the heated nozzle (~210 °C) with a diameter of 0.14 mm. The printing speed was set constant at 20 mm/s.
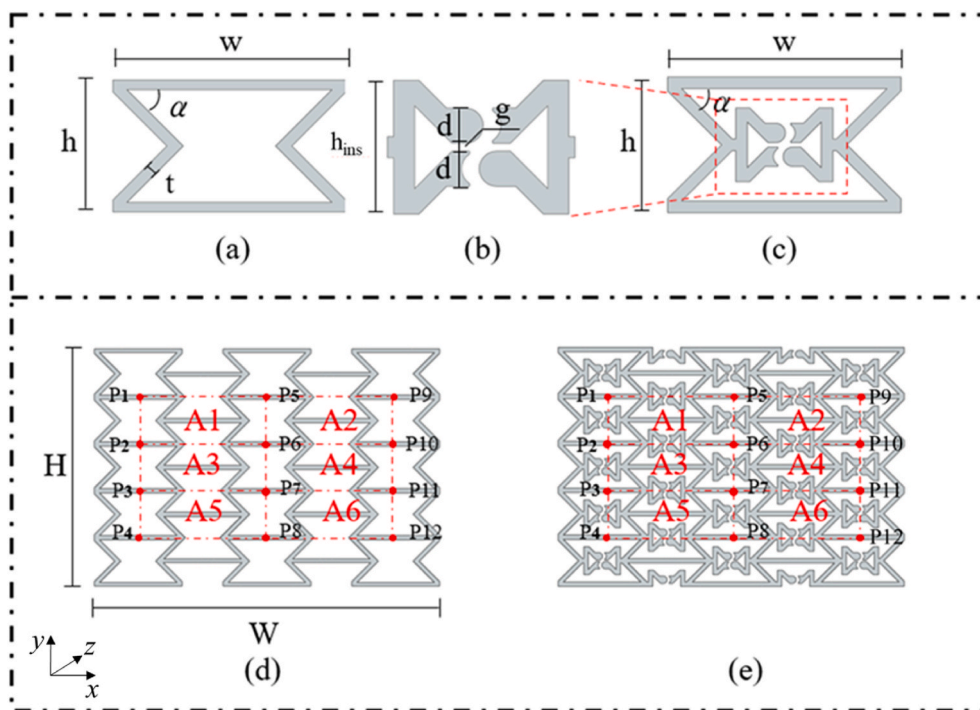
Fig. 1. Geometric schematics of the proposed structures: (a) CRS unit, (b) the enlarged view of the nested re-entrant unit, (c) SREAM unit, (d) CRS, and (e) SREAM-#.
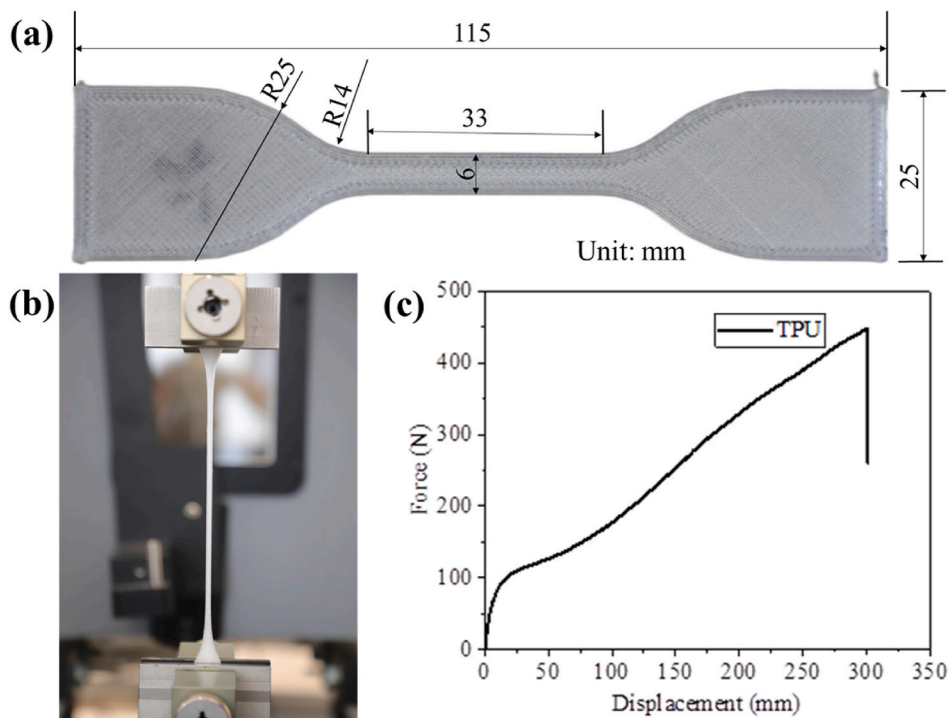

Fig. 2. Uniaxial tensile test on the TPU samples: (a) standard size of dumbbell-shape TPU samples, (b) uniaxial tensile test setup, and (c) the representative stress-strain curve of samples.

2.3. Quasi-static compression test

A quasi-static compression test was carried out using a universal testing machine (WANCE ETM-104 B, China) to investigate the mechanical performance of SREAM-# and CRS. A downward velocity load was applied to the specimens with a compression rate of 7.2 mm/min. The test was aborted until it reached a total compression distance of 60 mm. The deformation behavior was tracked by a digital Camera [55], while the stress-strain curves were automatically recorded by the controller of the testing machine.

2.4. Numerical simulation

To verify experimental results, the mechanical behavior of the pro-

posed SREAM and CRS were also compared and analyzed via a numerical simulation method by the commercial finite element software Abaqus. An Explicit analysis was conducted. The hyperelastic model of TPU in Fig. 2(c) was entitled to the instance where it was meshed by the 8-node linear brick element with reduced integration (C3D8R). Subsequently, the meshed models were placed between two analytical rigid plates. The general contact [54] was employed in the aforesaid models, with the normal behaviors as 'Hard' contact and tangential behaviors frictionless of 0.2, respectively. A reference point [56] was then set in the center of the top rigid plate and assigned a 'Kinetic Coupling' constraint to collect the reaction force (F) of the structure along with loading. The downward velocity load was applied on the reference point via a compression rate (v_{load}) of 7.2 mm/min and lasted until reaching a total displacement of 60 mm. In this study, the nominal strain was defined as $\varepsilon = \Delta H/H = v_{load}t/H$, where H (~120 mm) is the original height of structures. Similarly, the nominal stress can be obtained via $\sigma = F/A$, where A was the area of the top surface.

2.5. Poisson's ratio calculation

To calculate the Poisson's ratio of both structures, totally 12 label Points were marked on the fabricated structures, as illustrated in Fig. 1, and their displacement information was thus obtained. According to an image processing method, the computing equations of the equivalent Poisson's ratio are shown in formulas (1-8):

$$v_{A1} = -\frac{\varepsilon_{A1}^x}{\varepsilon_{A1}^y} \tag{1}$$

where v_{A1} is the Poisson's ratio of the labeled area $A1$, ε_{A1}^x and ε_{A1}^y are the average strain of $A1$ in the transverse direction (X-axis direction) and vertical direction (Y-axis direction).

$$\varepsilon_{A1}^x = \frac{\Delta U_1}{U_1} \tag{2}$$

$$\Delta U_1 = \frac{[(x_5 - X_5) + (x_6 - X_6)] - [(x_1 - X_1) + (x_2 - X_2)]}{2} \tag{3}$$

$$U_1 = \frac{X_5 + X_6 - X_1 - X_2}{2} \tag{4}$$

where ΔU_1 is the average transverse deformation of the labeled area $A1$, x_j is the instantaneous x coordinate of point P_j, X_j is the original x coordinate of point P_j, and U_1 is the original length of $A1$ in the transverse direction.

Similarly, the vertical strain of labeled area $A1$ can be defined as follows.

$$\varepsilon_{A1}^y = \frac{\Delta V_1}{V_1}, \tag{5}$$

$$\Delta V_1 = \frac{[(y_1 - Y_1) + (y_5 - Y_5)] - [(y_2 - Y_2) + (y_6 - Y_6)]}{2}, \tag{6}$$

$$V_1 = \frac{Y_1 + Y_5 - Y_2 - Y_6}{2}, \tag{7}$$

where ε_{A1}^y is the vertical strain of labeled area $A1$, y_j and Y_j demonstrate the instantaneous y coordinate and original y coordinate of point P_j, respectively.

And the Poisson's ratio of the whole structure in Fig. 1 can be defined as

$$v = \frac{1}{6}\Sigma v_{Ai}, (1 \leq i \leq 6), \tag{8}$$

where v_{Ai} represents the Poisson's ratio of labeled area A_i.

2.6. Geometric optimization

According to the geometric design of SREAMs, several geometric parameters may determine their configurations, further, the mechanical performance. In this way, it is necessary to explore the effects of the key parameters of SREAMs to help optimize structural designs. Several main geometric parameters, namely, the thickness, the height, the lateral pitch, and connections of inner re-entrants for SREAMs, are thus selected and concerned, as illustrated in Fig. 3(a). In Table 1, a total of 8 SREAM samples have been proposed, which conclude the variable parameters and their corresponding relative density.

The relative density of porous SREAMs can be determined by Eq. (9).

$$\rho = \frac{V_{SRE}}{V_{mat}} \tag{9}$$

where V_{SRE} is the volume of SREAMs listed in Table 1, V_{mat} is the matrix's volume, and $V_{mat} = 1296000$ mm³ in this study.

To investigate the influence of inner re-entrant connection, a fixed joint inner re-entrant based SREAM sample, namely, the SREAM-CO, has also been presented in Fig. 3(b). Herein, the auxeticity and deformation patterns were further studied via the numerical method according to Sections 2.4 and 2.5.

3. Results

3.1. Deformation behaviour

Fig. 4 demonstrates the deformation pattern and strain distribution of the above structures under compression, with the nominal strain growing from 0 to 0.5. It is easy to recognize that experimental and numerical results show good consistency for both CRS and SREAM, in which the SREAM presents better mechanical stability than CRS.
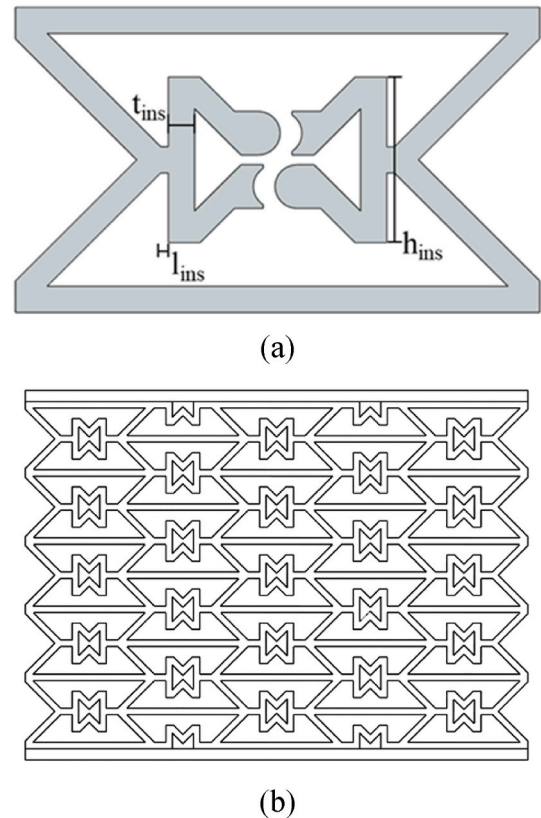

(a)

(b)

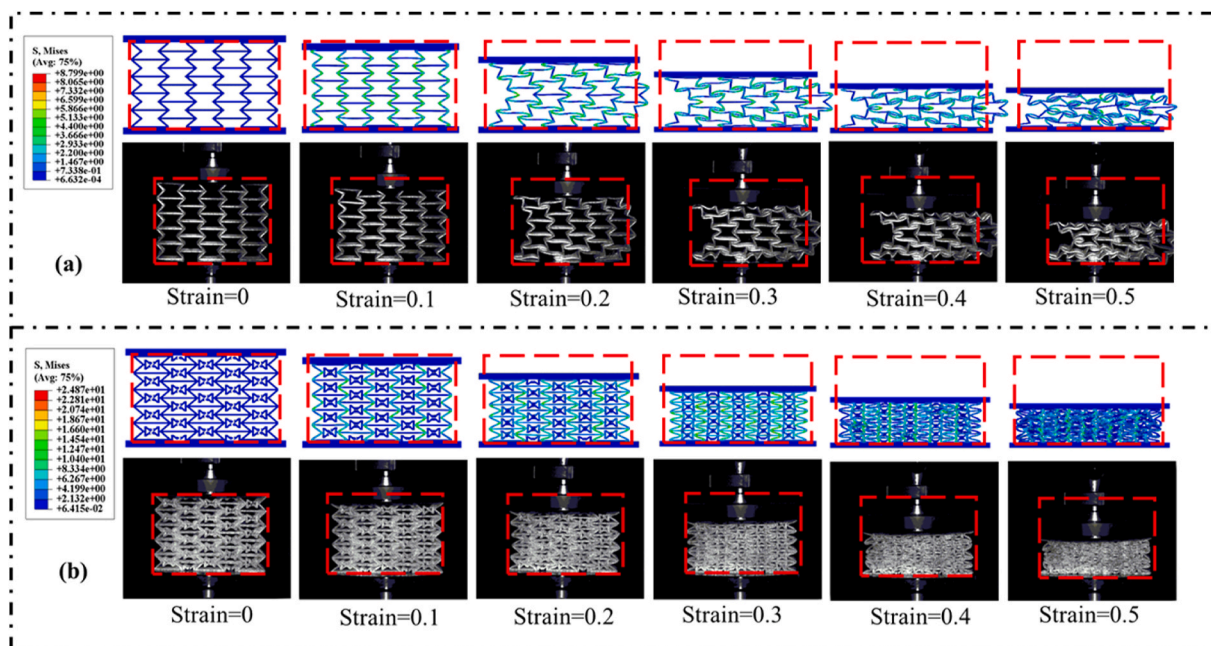**Fig. 3.** Schematics of SREAMs: (a) typical geometric parameters, (b) SREAM-CO.

Fig. 4. Deformation behavior of the structures during compression process: (a) CRS, and (b) SREAM.

Table 1
The parameter investigation of SREAMs.

Samples	t_{ins} (mm)	l_{ins} (mm)	h_{ins} (mm)	(mm^3)	ρ	E_1 (MPa)	E_2 (MPa)	E_3 (MPa)
SREAM-#	2.29	0.67	14.49*	533144.05	0.4114	0.244	9.931	20.029
CRS	–	–	–	290843.37	0.2244	0.157	0.040	0.520
SREAM-T1	1	0.67	14.49*	422911.70	0.3263	0.179	8.256	16.230
SREAM-T3	3	0.67	14.49	578165.84	0.4461	0.327	12.667	20.292
SREAM-L0	2.29	0	14.49	527054.99	0.4067	0.176	8.426	16.230
SREAM-L1.43	2.29	1.43	14.49	537925.87	0.4151	0.366	12.761	16.720
SREAM-H14	2.29	0.67	14	530107.36	0.4090	0.232	8.882	16.125
SREAM-H18	2.29	0.67	18	556704.09	0.4296	0.284	12.559	20.287
SREAM-CO	2.29	2	14.49	502199.75	0.3875	0.205	0.862	6.499

Specifically, the CRS shows obvious buckling after strain reaching around 0.1, and its asymmetric transverse deformation gradually increases with loading. Contrarily, from the deformed configurations (Fig. 4(b)), the proposed SREAM may show a more balanced deflection pattern than CRS, with almost symmetric deformation in the whole compression process. Such stable deformation patterns can be contributed to the geometric enhancement of the inserted re-entrants for SREAM. Two joint hinges of the nested re-entrants in SREAM transversely contacted and consequently compacted after strain = 0.1, in which more rugged triangular-like configurations present with better stiffness and firmness. Apart from better deformation behavior, the typical auxeticity of SREAM is another issue, as presented in Fig. 4(b). According to Fig. 4(b), we may see a slight lateral contraction under the compression, which rarely presents excessive buckling, suggesting superior structural stability. The auxetic property can be further quantified and analyzed in Section 3.3. Overall, the proposed SREAM shows a good mechanical response, namely, improved mechanical stability and auxeticity during the compression process.

3.2. Quasi-static compression properties

Fig. 5 reveals typical quasi-static compression properties of both CRS and the proposed SREAM, with each curve dividing into three distinct phases. According to Fig. 5(a), the stress-strain curve of CRS may consist of the elastic phase (0-P_{ela}), the plateau phase (P_{ela}-P_{plu}), and the densification phase [57]. The CRS firstly shows a liner elastic increase before

strain reaching around 0.078, suggesting an elastic deformation process in low strains. Afterward, it enters a typical plateau phase ranging from P_{ela} (strain 0.078) to P_{plu} (strain 0.293), where the stress remains nearly constant at around 0.035 MPa, but no obvious growth with strain. The unstable deformation, namely, buckling of CRS, as presented in Fig. 4 (a), may contribute to the aforesaid plateau phase. In this phase, excessive lateral deformation greatly slows down the growth rate of stress. Eventually, the stress of CRS dramatically grows because it is compacted along with the compression process after it reaches P_{plu}. The dense structure of compact CRS thus offers higher stuffiness, rising in stress in the densification phase.

The SREAM may show a different closure phase, although it includes a similar elastic phase (0-P_{con}) and densification phase (after P_{cat}) with CRS. Different from the plateau phase of CRS, a slight increase can be seen from the start point P_{con} (strain 0.109) to the end point P_{cat} (strain 0.266) in the closure phase (Fig. 5(b)), suggesting a mildly increased stiffness of SREAM. It can be illustrated that the compaction process of the inner re-entrants may increase the transitive stiffness starting from the two hinges transversely contact (P_{con}) to vertical compact (P_{cat}), with the deformation process of nested blades in Fig. 5 (b). After the two blades compact, the inner self-similar re-entrants are eventually completed, which almost increases the geometric symmetry and transverse stiffness, thus avoiding unstable buckling (Fig. 4). It is then quickly compressed into dense after strain reaching 0.266 at P_{cat}. Finally, in the densification phase, the earlier densification and much higher stress in Fig. 5(b) can be contributed to a denser geometric
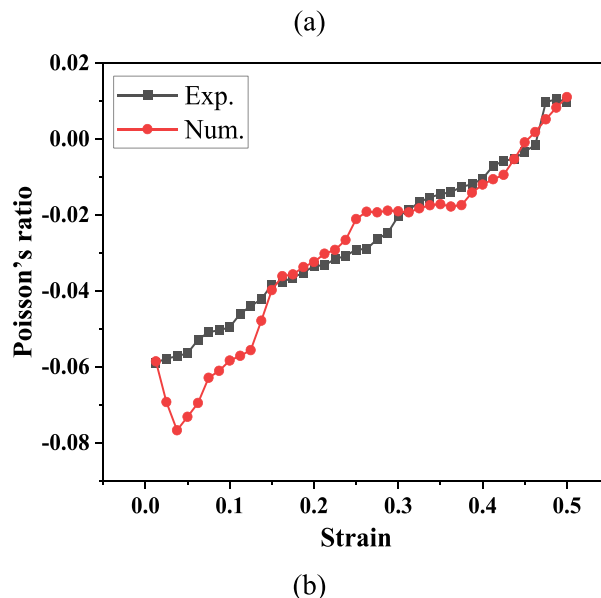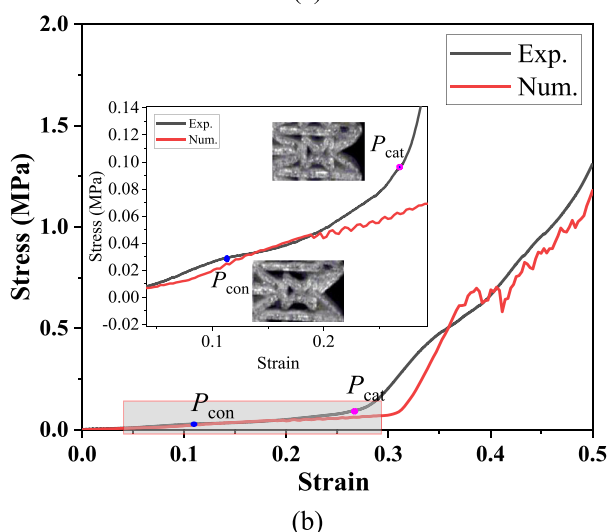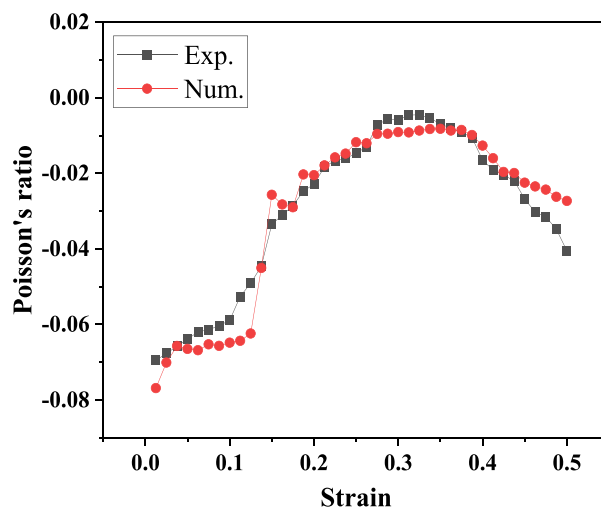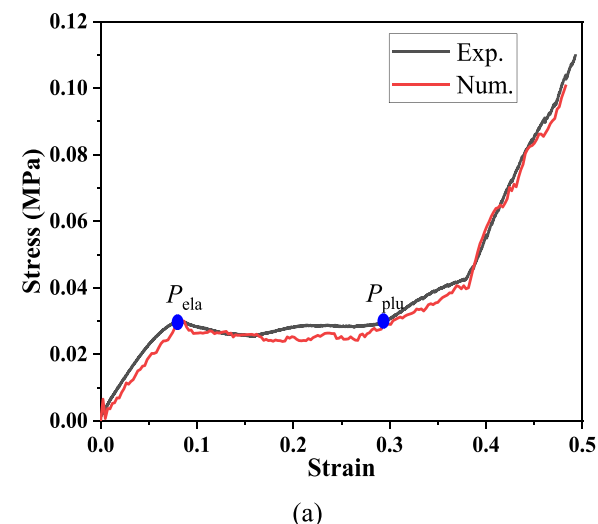
(a)

(b)

Fig. 5. Nominal stress-strain responses of two kind of structures: (a) CRS, and (b) SREAM.

(a)

(b)

Fig. 6. Poisson's ratios of two kinds of structures: (a) CRS, and (b) SREAM.

schematic of SREAM than CRS. The results reveal that the SREAM shows a higher stiffness and better stability, especially along with the formation of self-similar inner re-entrants in the closure phase and densification.

Generally, it may present a generally similar trend between the numerical and experimental results in Fig. 5, which verified the consistency of the above results. There are still some differences between experimental and numerical results, as illustrated in Fig. 5. According to Fig. 5, it can be seen some fluctuations occurred in the numerical results, especially after the strain reached around 0.372. These errors are mainly caused by anisotropy for the samples prepared via the 3D printing technique which may fail to conform to the assumption of homogeneity. Specifically, the interlayer defects and pores during the printing process cannot be avoided, which disrupts the homogeneity of produced specimens on a micro/macro scale. Besides, the samples produced via additive manufacturing technology will lead to great anisotropy due to different printing paths, which inevitably make the mechanical properties different between experimental and numerical results. Similar errors may generally be reported in previous research [54].

3.3. Auxeticity

Fig. 6 presents Poisson's ratio of both CRS and the proposed SREAM. It is easy to recognize that the experimental results show good

consistency with numerical ones. For CRS, the Poisson's ratio increased dramatically when the strain reached around 0.138 in Fig. 6(a), suggesting a declined auxeticity caused by buckling. It can also be verified in Fig. 4(a), where buckling happens at strain ~0.1. When the structure tends to be compact, the general Poisson's ratio approximates zero when the transverse deformation is gradually restored.

Contrarily, the SREAM may obtain a general increase in Poisson's ratio with rare fluctuations in Fig. 6(b). The difference is due to the enhanced the overall stiffness of SREAM [54], which helps avoid structure buckling. It could be judged via both the equivalent Young's modulus and Maxwell's stability criterion [58–61]. According to Table 1, the equivalent Young's modulus of SREAM is generally higher than that of CRS. For instance, the E_2 of SREAM-# reaches around 9.931 MPa, much higher than that of CRS (~0.040 MPa). Such enhanced stiffness may help the structure avoid the possible buckling referring to the deformation mode as presented in Fig. 4(b). The relative smooth curve in Fig. 6(b) may demonstrate a stable deformation response due to the addition of nested re-entrants. Similar to CRS, SREAM keeps its auxeticity during the compression process, although the negative value almost vanishes at the end.

The results may verify that SREAM keeps its instinct auxeticity, mainly because it can almost avoid confusion from buckling.

3.4. Stiffness

The stiffness enhancement of SREAMs can be characterized by a typical metric, namely, the equivalent Young's modulus (E_i) of SREAMs. It can be defined as the slope of the stress-strain curves in their three strain phases, i.e., elastic phase, closure, and densification. The equivalent Young's modulus for the three phases is listed in Table 1 and remarked as E_1, E_2, and E_3, respectively.

It is also highly expected that the denser structures may have relatively higher stiffness, making it difficult to evaluate or compare their mechanical performance directly. In this way, it is significant to compare the mechanical performance between CRS and SREAM in their relative density regard. And this study thus establishes a metric, namely, the relative Young's modulus factor (YF_i), comparing the stiffness difference while excluding the effect of different relative densities.

The definition of YF_i can be presented as follows:

$$YF_i = \frac{E_i}{\rho} \tag{10}$$

where E_i is the equivalent Young's modulus in three phases, i ~1, 2 and 3, and ρ is the relative density of CRS or SREAM. Fig. 7 presents the relative Young's modulus factor of CRS and SREAM with their relative density (ρ) ~ 0.224 and 0.411, respectively. It can be easily recognized that the SREAM obtains a higher YF_i than that of CRS in each strain phase, suggesting a superior stiffness enhancement efficiency when adding more extra geometry in the CRS. The gap of YF_i on CRS and SREAM is dramatically widening especially on the YF_2 and YF_3, where the YF_3 of SREAM (~48.685 MPa) is more than 43 times that of CRS (~2.317 MPa). On the contrary, the CRS and SREAM have rare differences on YF_1, keeping a relatively constant value at around 0.59 MPa. The increasing gap demonstrates that the relative density mainly positively influences the closure and densification phases.

The aforesaid analysis indicates that the SREAM obtains higher stiffness per volume than CRS, suggesting its higher efficiency on keeping structural stability.

4. Discussion

4.1. Parameter investigation

4.1.1. The effect of inner re-entrant thickness (t_{ins})

Fig. 8 reveals the effect of inner re-entrant thickness (t_{ins}) on the corresponding SREAMs' mechanical behavior. As shown in Fig. 8(a), all the SREAMs follow similar patterns on Poisson's ratio, declining before
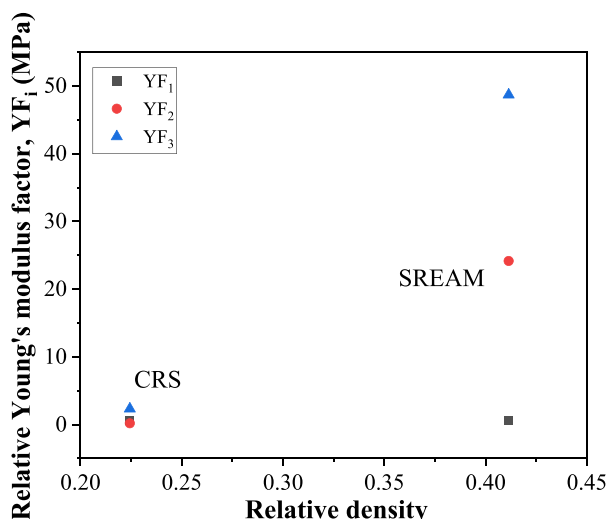

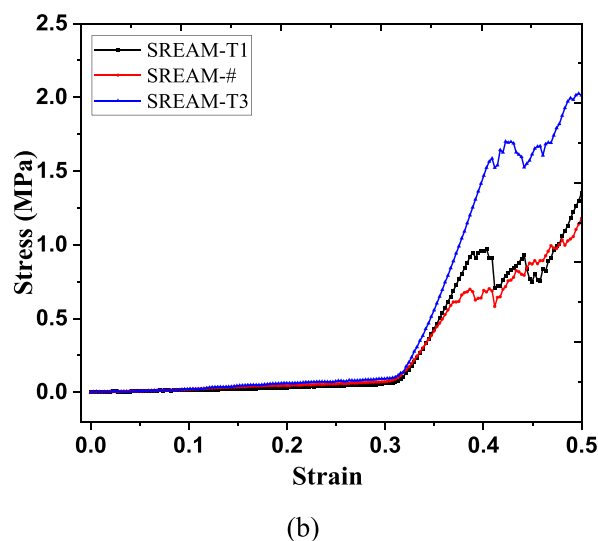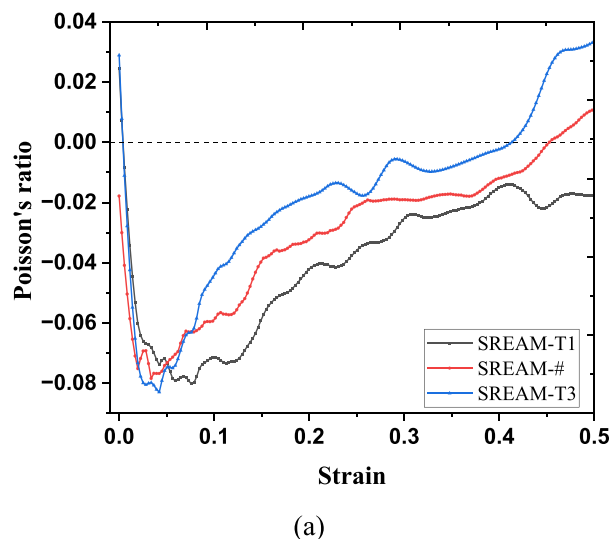Fig. 7. The relative Young's modulus factor.

(a)

(b)

Fig. 8. The effect of inner re-entrant thickness: (a) Poisson's ratio (b) Stress-strain response.

the strain at around 0.02 and finally growing along with the loading process. Similarly, almost all SREAMs show good auxeticity before the strain reaches 0.41. However, the thinner inner re-entrants (SREAM-T1) may be prone to endure its auxeticity compared with a thickness of 3 mm (SREAM-T3), where it almost maintains negative Poisson's ratios during the loading process. Furthermore, the Poisson's ratio values of all the proposed SREAMs are inversely proportional to the inner re-entrant's thickness. In summary, the higher thickness may be not good for the SREAM's auxeticity, although it may increase the stiffness and strength of the structure, as shown in Fig. 8(b). The dramatically increasing strength of SREAM-T3 can be attributed to a denser structure with a density of 0.4461, where it is easier and earlier to be totally compacted in the densification phase.

Table 1 shows the effect of t_{ins} on the equivalent Young's modulus in terms of SREAM-T1, -#, and -T3. Each SREAM specimen's equivalent Young's modulus may exhibit an increasingly dramatic trend over the course of the three strain phases, indicating a pronounced stiffness improvement. Compared with SREAM-#, the denser inner re-entrant thickness of SREAM-T3 may lead to a universal improvement, with the values of E_1, E_2, and E_3 increasing at around 0.327, 12.667 and 20.292, respectively. The boosted equivalent Young's modulus can be accounted for the higher relative density (ρ) of SREAM-T3, whose stress distribution has been proven to show a consistent increase with the

equivalent Young's modulus, as seen in Fig. 8(b).

In summary, the higher t_{ins} may benefit the overall stiffness while suppressing the auxeticity, suggesting it is a tendentious factor for adjusting the performance of SREAMs.

4.1.2. The effect of inner re-entrant height (h_{ins})

Fig. 9 presents the mechanical effect of inner re-entrant height (h_{ins}) on the proposed SREAMs. Compared with those with lower heights, the higher inner re-entrant (SREAM-H18) may show obviously lower Poisson's ratios before the strain reaches around 0.48, and it subsequently grows to around 0.04601 in the end. The aforesaid difference may be
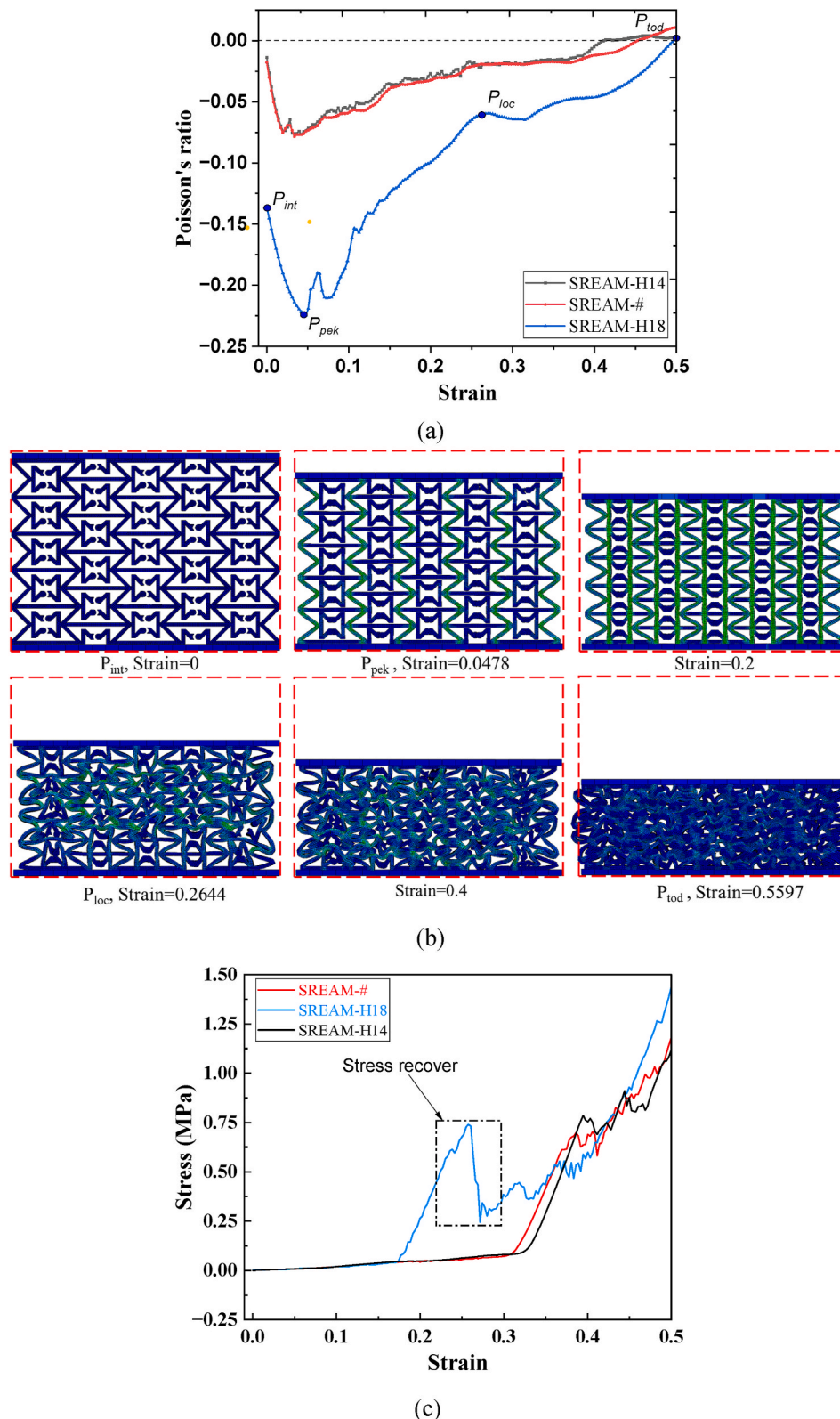

(a)

(b)

(c)

Fig. 9. The effect of inner re-entrant height: (a) Poisson's ratio, (b) deformation patterns of SREAM-H18, and (c) stress-strain response.

also verified via the deformation patterns in Fig. 9(a), where four typical moments were especially concerned, namely the initial point (P_{int}), Peak point (P_{pek}), local collapse point (P_{loc}), and Total densification point (P_{tod}). It can be identified that at the Peak point (P_{pek}), the vertical inner hinges may be contacted with outer re-entrants before their transverse hinges contract with each other. Afterward, an approximately stable structure composed of simplified triangles (as illustrated in Fig. 9(b)) was subsequently formed, which obtained higher stiffness and strength. It may further hinder the auxeticity of SREAM-H18, where the Poisson's ratio increased quickly from -0.22468 to -0.06035 at the local collapse point (P_{loc}). In the end, the continued local collapse may lead to an acceleration of structure degradation, with Poisson's ratio rising rapidly to around 0.04601 at P_{tod}. Contrarily, there are much the same in Poisson's ratios between SREAM-H14 and SREAM-# because of a slight difference in thickness.

Fig. 9(c) demonstrates the stress-strain response of the SREAMs with three different h_{ins}. It can be recognized that the stress is generally proportional to the h_{ins} compared with SREAM-H18, -H14, and -# in Fig. 9(c). There are similar trends in the curves of SREAM-# and SREAM-H14 due to rare differences in inner re-entrant height. However, it seems to show an earlier closure phase after the strain reaches around 0.174 when it turns to SREAM-H18, with the slope of the curve increasing dramatically in Fig. 9(c). The earlier closure phase of SREAM-H18 mainly contributes to the earlier vertical compaction of the inner re-entrant core, where its vertical blades may quickly contact the transverse edges of outer re-entrants along with the loading process. After the quick closure, the strain may quickly fall and gradually recover after strain ~0.257, as remarked in the dotted box in Fig. 9(c). The reduced strain is mainly caused by the local collapse of the above vertical wedges in the nested re-entrants. After that, it goes into a densification phase whose strain grows dramatically with an increased relative density. In this way, the higher h_{ins} may benefit the strength of SREAMs due to earlier closure.

The stiffness enhancement of specimens with different inner heights (h_{ins}), namely, SREAM-H14, SREAM-#, and SREAM-H18 are further compared according to Table 1. It can be identified that the equivalent Young's modulus grows in line with h_{ins}, where the E2 of SREAM-H18 grows to around 12.559 MPa compared with that of 8.882 MPa in SREAM-H14. The consistent growth of the equivalent Young's modulus can be attributed to the earlier vertical contract of inner re-entrant spans in SREAM-H18.

In this way, the increasing inner re-entrant height may help SREAM obtain a clear auxetic effect with a higher absolute peak value because it may form relatively stable structures composed of simplified triangle structures during the deformation process.

Overall, the h_{ins} shows the typical promoting effects on both auxeticity and stiffness. Specifically, it is proportional to the stiffness and the auxeticity of SREAMs simultaneously.

4.1.3. The effect of the lateral pitch of inner re-entrants (l_{ins})

The effect of the inner re-entrant's lateral pitch (l_{ins}) can be shown in Fig. 10. Total of three SREAMs with different lateral pitches was selected and compared, namely SREAM-L0, SREAM-#, and SREAM-L1.43. According to Fig. 10(b), there were little different trends among these samples, suggesting it may show less influence on stress distribution. Apart from the stress-strain curves, the SREAM-L0 may obtain generally higher Poisson's ratio than SREAM-# and SREAM-L1.43 in Fig. 10(a). It indicated that Poisson's ratio values were inversely proportional to the lateral pitch.

Besides, it is easy to recognize that the l_{ins} is proportional to the equivalent Young's modulus compared with the samples with various inner re-entrant lateral pitches, such as SREAM-L0, SREAM-#, and SREAM-L1.43. For instance, the values of E_1 may range from 0.176 to 0.366, along with the increased l_{ins} from 0 to 1.43 mm, as illustrated in Table 1. As a result, increasing the value of l_{ins} is also one of the effective
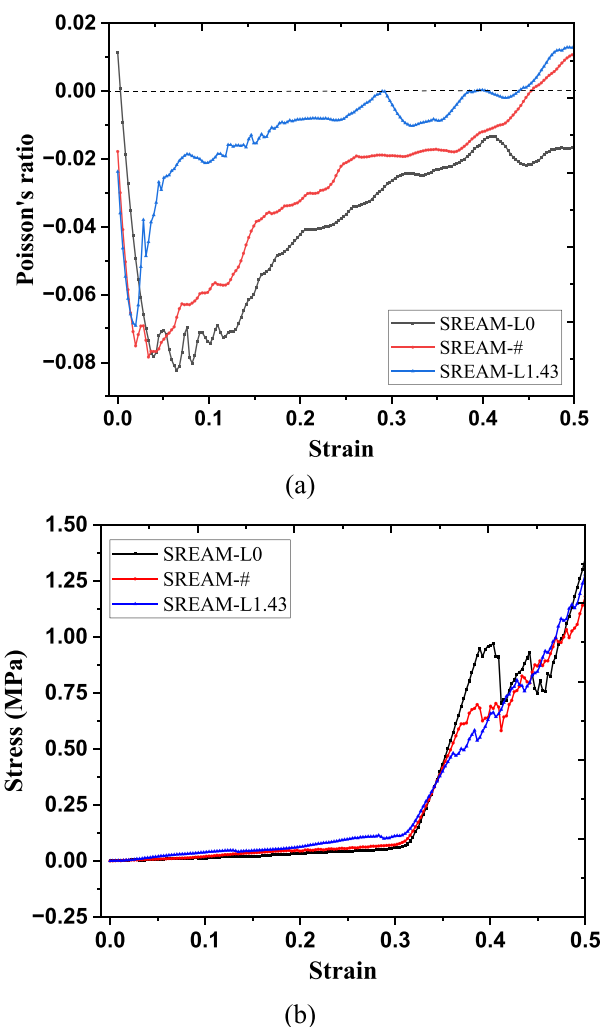

(a)

(b)

Fig. 10. The effect of the lateral pitch of inner re-entrants: (a) Poisson's ratio, (b) Stress-strain curves.

means to boost the overall stiffness.

It has been proven that the l_{ins} is also a key factor which may positively boost the overall stiffness while limiting the NPR of the proposed SREAMs.

4.2. The effect of connection

The fixed joint of the inner re-entrant in the SREAM structure was also studied. As is shown in Fig. 11(a), the fixed joint has been proven to show better auxeticity, whose Poisson's ratios were generally lower than SREAM-#. It may be accounted that the fixed joint method could help the SREAM structure benefit from higher geometric integrity, thus, better performance in auxeticity. However, such fixed joints may fail to improve the transverse stiffness, which causes more obvious buckling, as illustrated in Fig. 11(b). There was serve buckling at the strain reaching around 0.1 from Fig. 11(b), suggesting an unstable deformation pattern. Compared with the relatively stable deformation patterns in Fig. 4(b), SREAM-CO may appear premature asymmetric deformations which would do harm in conditions where balanced boundaries are necessary.

To sum up, the fixed joint of inner re-entrants in SREAM may help obtain better auxeticity due to improved geometric integrity. However, it may fail to eliminate buckling, as verified by its unstable deformation patterns after being compared with SREAM-#.
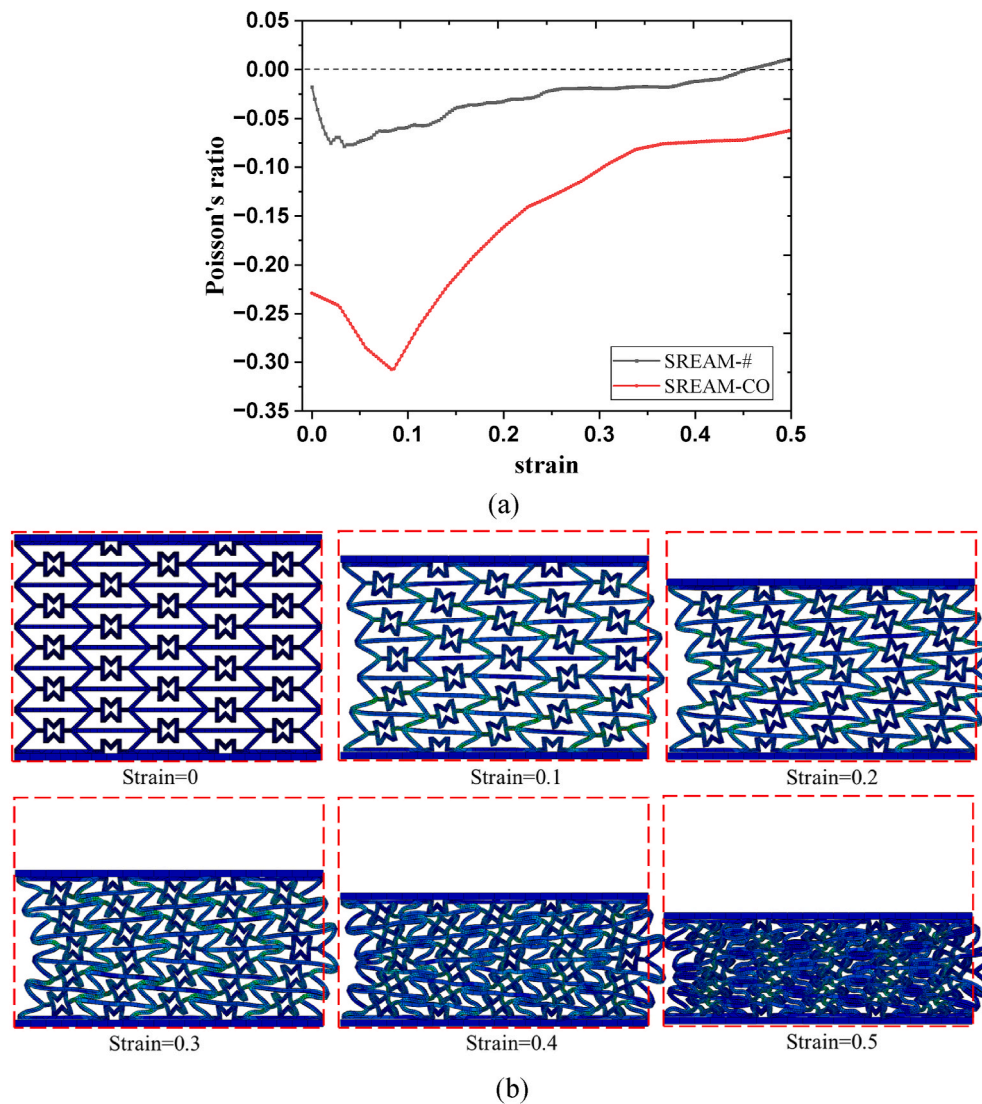
Fig. 11. The effect of connection: (a) the Poisson's ratio, (b) the deformation patterns.

5. Conclusion

This paper proposed a type of hybrid self-similar re-entrant auxetic metamaterial (SREAM). The compression properties, namely, auxeticity and stress-strain response, were investigated via both numerical analysis and experimental tests. The main geometric parameters in the inner-re-entrant part have thus been discussed to explore their effects on the mechanical behaviour and further optimize their geometries, especially the auxeticity, deformation patterns, and stress-strain response. The main conclusions can be summarized as follows:

(1) The proposed SREAMs achieve a good balance between the tunable stiffness and auxeticity. Compared with CRS, SREAMs obtain superior mechanical stability due to enhanced stiffness while maintaining the relatively good negative Poisson's ratio property.

(2) The three-phase stress-strain response is obtained for SREAMs, which consists of the elastic phase, closure, and total densification. The enhanced stiffness of SREAM in the above phases has been verified via both the equivalent Young's modulus and the relative Young's modulus factor, in their absolute and relative density regards, respectively.

(3) The parameters, such as lateral pitch and the thickness of inner re-entrants are proportional to overall stiffness while reversely related to their auxeticity. Contrarily, the increased inner re-entrant's height may promote its auxeticity and stiffness simultaneously.

(4) The fixed joint of inner re-entrants is proven to show serve buckling, although it may present good auxetic performance.

Author statement

Peng Dong: Methodology, Formal analysis, Writing. Runsheng Hou: Editing, Writing, Investigation. Jiayi Hu: Methodology, Investigation. Chen Lin: Formal analysis, Writing. Yuqing Liu: Conceptualization, Funding acquisition, Supervision, Project administration. Lei Qin: Methodology, Supervision, Project administration.

Declaration of competing interest

The authors declare that they have no known competing financial interests or personal relationships that could have appeared to influence the work reported in this paper.

Data availability

Data will be made available on request.

Acknowledgments

The authors would like to acknowledge the funding support from the Science, Technology and Innovation Commission of Shenzhen Municipality (grant no. ZDSYS20210623092005017).

References

[1] R. Yu, W. Luo, H. Yuan, et al., Experimental and numerical research on foam filled re-entrant cellular structure with negative Poisson's ratio, Thin-Walled Struct. 153 (2020), 106679.
[2] N.S. Ha, T.M. Pham, T.T. Tran, et al., Mechanical properties and energy absorption of bio-inspired hierarchical circular honeycomb, Compos. B Eng. 236 (2022), 109818.
[3] Z. Dong, Y. Li, T. Zhao, et al., Experimental and numerical studies on the compressive mechanical properties of the metallic auxetic reentrant honeycomb, Mater. Des. 182 (2019), 108036.
[4] R. Zhong, X. Ren, X. Yu Zhang, et al., Mechanical properties of concrete composites with auxetic single and layered honeycomb structures, Construct. Build. Mater. 322 (2022), 126453.
[5] Y. Jiang, Y. Li, 3D printed chiral cellular solids with amplified auxetic effects due to elevated internal rotation, Adv. Eng. Mater. 19 (2017), 1600609.
[6] R. Hamzehei, S. Rezaei, J. Kadkhodapour, et al., 2D triangular anti-trichiral structures and auxetic stents with symmetric shrinkage behavior and high energy absorption, Mech. Mater. 142 (2020), 103291.
[7] Y. Fan, H. Shen, Non-symmetric stiffness of origami-graphene metamaterial plates, Compos. Struct. 297 (2022), 115974.
[8] Q. Li, X. Zhi, F. Fan, Quasi-static compressive behaviour of 3D-printed origami-inspired cellular structure: experimental, numerical and theoretical studies, Virtual Phys. Prototyp. 17 (2022) 69–91.
[9] N. Novak, L. Starčevič, M. Vesenjak, et al., Blast response study of the sandwich composite panels with 3D chiral auxetic core, Compos. Struct. 210 (2019) 167–178.
[10] X. Zhang, X. Ren, W. Jiang, et al., A novel auxetic chiral lattice composite: experimental and numerical study, Compos. Struct. 282 (2022), 115043.
[11] S. Mohsenizadeh, R. Alipour, M. Shokri Rad, et al., Crashworthiness assessment of auxetic foam-filled tube under quasi-static axial loading, Mater. Des. 88 (2015) 258–268.
[12] S. Jin, Y.P. Korkolis, Y. Li, Shear resistance of an auxetic chiral mechanical metamaterial, Int. J. Solid Struct. 174–175 (2019) 28–37.
[13] K.K. Dudek, R. Gatt, J.N. Grima, 3D composite metamaterial with magnetic inclusions exhibiting negative stiffness and auxetic behaviour, Mater. Des. 187 (2020), 108403.
[14] X. Cheng, Y. Zhang, X. Ren, et al., Design and mechanical characteristics of auxetic metamaterial with tunable stiffness, Int. J. Mech. Sci. 223 (2022), 107286.
[15] D. Da, Y. Chan, L. Wang, et al., Data-driven and topological design of structural metamaterials for fracture resistance, Extreme Mechanics Letters 50 (2022), 101528.
[16] T. Kuşkun, J. Smardzewski, A. Kasal, Experimental and numerical analysis of mounting force of auxetic dowels for furniture joints, Eng. Struct. 226 (2021), 111351.
[17] H.M.A. Kolken, S. Janbaz, S.M.A. Leeflang, K. Lietaert, H.H. Weinans, A. A. Zadpoor, Rationally designed meta-implants: a combination of auxetic and conventional meta-biomaterials, Mater. Horiz. 5 (2018) 28–35.
[18] Q. Gao, X. Zhao, C. Wang, et al., Multi-objective crashworthiness optimization for an auxetic cylindrical structure under axial impact loading, Mater. Des. 143 (2018) 120–130.
[19] M. Ghafouri, M. Ghassabi, M.R. Zarastvand, et al., Sound propagation of three-dimensional sandwich panels: influence of three-dimensional re-entrant auxetic core, AIAA J. 60 (11) (2022) 6374–6384.
[20] W. Liu, N. Wang, T. Luo, Z. Lin, In-plane dynamic crushing of re-entrant auxetic cellular structure, Mater. Des. 100 (2016) 84–91.
[21] C. Qi, L. Pei, A. Remennikov, S. Yang, F. Jiang, Numerical and theoretical analysis of crushing strength of 3D re-entrant honeycomb, Thin-Walled Struct. 182 (2023), 110140.
[22] W. Zhang, Z. Li, J. Wang, F. Scarpa, X. Wang, Mechanics of novel asymmetrical re-entrant metamaterials and metastructures, Compos. Struct. 291 (2022), 115604.
[23] R.S. Dhari, Z. Javanbakht, W. Hall, On the deformation mechanism of re-entrant honeycomb auxetics under inclined static loads, Mater. Lett. 286 (2021), 129214.
[24] C. Qi, F. Jiang, A. Remennikov, L. Pei, J. Liu, J. Wang, X. Liao, S. Yang, Quasi-static crushing behavior of novel re-entrant circular auxetic honeycombs, Compos. B Eng. 197 (2020), 108117.
[25] H. Wang, Z. Lu, Z. Yang, X. Li, A novel re-entrant auxetic honeycomb with enhanced in-plane impact resistance, Compos. Struct. 208 (2019) 758–770.
[26] F. Usta, H.S. Türkmen, F. Scarpa, High-velocity impact resistance of doubly curved sandwich panels with re-entrant honeycomb and foam core, Int. J. Impact Eng. 165 (2022), 104230.
[27] X. Cheng, Y. Zhang, X. Ren, et al., Design and mechanical characteristics of auxetic metamaterial with tunable stiffness, Int. J. Mech. Sci. 223 (2022), 107286.
[28] X.Y. Zhang, X. Ren, Y. Zhang, Y.M. Xie, A novel auxetic metamaterial with enhanced mechanical properties and tunable auxeticity, Thin-Walled Struct. 174 (2022), 109162.
[29] X.L. Ruan, J.J. Li, X.K. Song, et al., Mechanical design of antichiral-reentrant hybrid intravascular stent, International Journal of Applied Mechanics 10 (2018), 1850105.
[30] H. Lu, X. Wang, T. Chen, Enhanced stiffness characteristic and anisotropic quasi-static compression properties of a negative Poisson's ratio mechanical metamaterial, Thin-Walled Struct. 179 (2022), 109757.
[31] W. Zhang, S. Zhao, F. Scarpa, et al., In-plane mechanical behavior of novel auxetic hybrid metamaterials, Thin-Walled Struct. 159 (2021), 107191.
[32] F. Franco-Martínez, C. Grasl, E. Kornfellner, et al., Hybrid design and prototyping of metamaterials and metasurfaces, Virtual Phys. Prototyp. 17 (2022) 1031–1046.
[33] R. Hou, P. Dong, Y. Liu, Novel lozenge-chiral auxetic metamaterials (LCAMs): design and numerical studies, Mater. Lett. 331 (2023), 133440.
[34] P. Fan, Y. Chen, J. Xiong, et al., In-plane mechanical properties of a novel hybrid auxetic structure, Smart Mater. Struct. 31 (7) (2022), 075003.
[35] M.H. Fu, Y. Chen, L.L. Hu, A novel auxetic honeycomb with enhanced in-plane stiffness and buckling strength, Compos. Struct. 160 (2017) 574–585.
[36] K. Peliński, J. Smardzewski, Static response of synclastic sandwich panel with auxetic wood-based honeycomb cores subject to compression, Thin-Walled Struct. 179 (2022), 109559.
[37] R.P. Bohara, S. Linforth, T. Nguyen, et al., Dual-mechanism auxetic-core protective sandwich structure under blast loading, Compos. Struct. 299 (2022), 116088.
[38] D.K. Pokkalla, L.H. Poh, S.T. Quek, Isogeometric shape optimization of missing rib auxetics with prescribed negative Poisson's ratio over large strains using genetic algorithm, Int. J. Mech. Sci. 193 (2021), 106169.
[39] Y. Sakai, M. Ohsaki, Optimization method for shape design of Auxetic Bending-Active Gridshells using discrete differential geometry, Structures 34 (2021) 1589–1602.
[40] M. Borovinšek, N. Novak, M. Vesenjak, et al., Designing 2D auxetic structures using multi-objective topology optimization, Mater. Sci. Eng., A 795 (2020), 139914.
[41] D. Qi, H. Yu, W. Hu, et al., Bandgap and wave attenuation mechanisms of innovative reentrant and anti-chiral hybrid auxetic metastructure, Extreme Mechanics Letters 28 (2019) 58–68.
[42] Y. Jiang, Y. Li, 3D printed auxetic mechanical metamaterial with chiral cells and re-entrant cores, Sci. Rep. 8 (1) (2018) 1–11.
[43] C. Qi, F. Jiang, S. Yang, A. Remennikov, S. Chen, C. Ding, Dynamic crushing response of novel re-entrant circular auxetic honeycombs: numerical simulation and theoretical analysis, Aero. Sci. Technol. 124 (2022), 107548.
[44] W. Liu, H. Li, J. Zhang, Y. Bai, In-plane mechanics of a novel cellular structure for multiple morphing applications, Compos. Struct. 207 (2019) 598–611.
[45] W. Zhang, Z. Li, J. Wang, F. Scarpa, X. Wang, Mechanics of novel asymmetrical re-entrant metamaterials and metastructures, Compos. Struct. 291 (2022), 115604.
[46] L. Shen, K. Wei, K. Yuan, C. Shi, Z. Li, Z. Wang, A novel metamaterial incorporating both auxeticity and thermal shrinkage, Int. J. Mech. Sci. 233 (2022), 107650.
[47] H. Mohammad, Yousuf, Wael Abuzaid, Maen Alkhader, 4D printed auxetic structures with tunable mechanical properties, Addit. Manuf. 35 (2020), 101364.
[48] X. Zhang, H. Hao, R. Tian, Q. Xue, H. Guan, X. Yang, Quasi-static compression and dynamic crushing behaviors of novel hybrid re-entrant auxetic metamaterials with enhanced energy-absorption, Compos. Struct. 288 (2022), 115399.
[49] W. Zhang, S. Zhao, F. Scarpa, J. Wang, R. Sun, In-plane mechanical behavior of novel auxetic hybrid metamaterials, Thin-Walled Struct. 159 (2021), 107191.
[50] C. Qi, F. Jiang, A. Remennikov, L.Z. Pei, J. Liu, J.S. Wang, X.W. Liao, S. Yang, Quasi-static crushing behavior of novel re-entrant circular auxetic honeycombs, Compos. B Eng. 197 (2020), 108117.
[51] W. Zhang, S. Zhao, F. Scarpa, J. Wang, R. Sun, In-plane mechanical behavior of novel auxetic hybrid metamaterials, Thin-Walled Struct. 159 (2021), 107191.
[52] H.B. Lin, H.T. Liu, M.R. An, In-plane dynamic impact behaviors of a self-similar concentric star honeycomb with negative Poisson's ratio, Mater. Today Commun. 33 (2022), 104474.
[53] H. Jiang, Y. Ren, Q. Jin, G. Zhu, Y. Hu, F. Cheng, Crashworthiness of novel concentric auxetic reentrant honeycomb with negative Poisson's ratio biologically inspired by coconut palm, Thin-Walled Struct. 154 (2020), 106911.
[54] X.Y. Zhang, X. Ren, Y. Zhang, Y.M. Xie, A novel auxetic metamaterial with enhanced mechanical properties and tunable auxeticity, Thin-Walled Struct. 174 (2022), 109162.
[55] I.F. Ituarte, N. Boddeti, V. Hassani, et al., Design and additive manufacture of functionally graded structures based on digital materials, Addit. Manuf. 30 (2019), 100839.
[56] H. Yang, B. Wang, L. Ma, Mechanical properties of 3D double-U auxetic structures, Int. J. Solid Struct. 180–181 (2019) 13–29.
[57] R.S. Dhari, Z. Javanbakht, W. Hall, On the deformation mechanism of re-entrant honeycomb auxetics under inclined static loads, Mater. Lett. 286 (2021), 129214.
[58] Z. Chen, X. Wu, Y.M. Xie, Z. Wang, S. Zhou, Re-entrant auxetic lattices with enhanced stiffness: a numerical study, Int. J. Mech. Sci. 178 (2020), 105619.
[59] N. Karathanasopoulos, H. Reda, J. Ganghoffer, Designing two-dimensional metamaterials of controlled static and dynamic properties, Comput. Mater. Sci. 138 (2017) 323–332.
[60] L.J. Gibson, M.F. Ashby, G.S. Schajer, C.I. Robertson, The Mechanics of Two-Dimensional Cellular Materials, vol. 382, Proceedings of the Royal Society of London, 1982, pp. 25–42.
[61] J.C. Maxwell, On the calculation of the equilibrium and stiffness of frames, London, Edinburgh Dublin Phil. Mag. J. Sci. 27 (1864) 294–299.